Efficient waveguide-integrated tunnel junction detectors at 1.6 μm

Philip C. D. Hobbs, Robert B. Laibowitz[*]**, Frank R Libsch,**
Nancy C. LaBianca, and Punit P. Chiniwalla[†]**,**

IBM T. J. Watson Research Center, PO Box 218, Yorktown Heights NY 10598
[*] *Department of Electrical Engineering, Columbia University, New York NY 10027*
[†] *Current address: School of Business, University of Michigan, Ann Arbor MI 48109*

pcdh@us.ibm.com

Abstract: Near-infrared detectors based on metal-insulator-metal tunnel junctions integrated with planarized silicon nanowire waveguides are presented, which we believe to be the first of their kind. The junction is coupled to the waveguide via a thin-film metal antenna feeding a plasmonic travelling wave structure that includes the tunnel junction. These devices are inherently broadband; the design presented here operates throughout the 1500-1700 nm region. Careful design of the antenna and travelling wave region substantially eliminates losses due to poor mode matching and *RC* rolloff, allowing efficient operation. The antennas are made from multilayer stacks of gold and nickel, and the active devices are Ni−NiO−Ni edge junctions. The waveguides are made via shallow trench isolation technology, resulting in a planar oxide surface with the waveguides buried a few nanometres beneath.The antennas are fabricated using directional deposition through a suspended Ge shadow mask, using a single level of electron-beam lithography. The waveguides are patterned with conventional 248-nm optical lithography and reactive-ion etching, then planarized using shallow-trench isolation technology. We also present measurements showing overall quantum efficiencies of 6% (responsivity 0.08 A/W at 1.605 μm), thus demonstrating that the previously very low overall quantum efficiencies reported for antenna-coupled tunnel junction devices are due to poor electromagnetic coupling and poor choices of antenna metal, not to any inherent limitations of the technology.

© 2007 Optical Society of America

OCIS codes: (040.3060) Detectors, infrared; (040.5570) Detectors, quantum; (130.2790) Guided waves; (240.7040) Tunnelling; (240.6680) Surface plasmons.

References and links

1. J. W. Dees, "Detection and harmonic generation in the sub-millimeter wavelength region," Microwave J. **9**, 48-55, 1966.
2. V. Daneu, D. Sokoloff, A. Sanchez, and A. Javan, "Extension of laser harmonic-frequency mixing techniques into the 9 μ region with an infrared metal-metal point contact diode," Appl. Phys. Lett. **15** (12), 398-401 (1969)
3. A. Sanchez, C. F. Davis, Jr., K. C. Liu, and A. Javan "The MOM tunneling diode: Theoretical estimate of its performance at microwave and infrared frequencies," J. Appl. Phys. **49**, 5270-5277 (1978)
4. M. Nagae, "Response time of metal-insulator-metal tunnel junctions," Japan. J. Appl. Phys. **11**, 1611-1621 (1972)
5. J. C. Martinez, and E. Polatdemir, "Measurement of tunneling time via electron interferometry," Appl. Phys. Lett. **84**, 8, 1320-1322 (2004)

6. C. Fumeaux, W. Herrmann, F. K. Kneubuehl, H. Rothuizen, B. Lipphardt, and C. O. Weiss, "Mixing of 28 THz (10.7 μm) CO2-laser radiation by nanometer thin-film Ni$-$NiO$-$Ni diodes with difference frequencies up to 176 GHz," Infrared Phys. Technol. **38**, 393-396 (1997)

7. S. Y. Wang, T. Izawa, T. K. Gustafson, "Coupling characteristics of thin-film metal-oxide-metal diodes at 10.6μm," Appl. Phys. Lett. **27**(9), 481-483 (1975)

8. I. Wilke, W. Herrmann, and F. K. Kneubuehl, "Integrated nanostrip dipole antennas for coherent 30 THz infrared radiation," Appl. Phys. **B58**, 87-95 (1994)

9. M. Abdel-Rahman, F. J. Gonzalez, G. Zummo, C. Middleton and G. D. Boreman, "Antenna-coupled MOM diodes for dual-band detection in MMW and LWIR," in *Radar Sensor Technology VIII and Passive Millimeter-Wave Imaging Technology VII*, R. Trebits, J. L. Kurtz, R. Appleby, N. Salmon, D. A. Wikner, Proc. SPIE **5410**, 238-243 (2004)

10. B. M. Kale, " Electron tunneling devices in optics," Opt. Eng. **24** (2), 267-274 (1985)

11. G. D. Boreman, A. Dogariu, C. C. Christodoulou, D. Kotter "Dipole-on-dielectric model for infrared lithographic spiral antennas," Opt. Lett. **21**(5), 309-311 (1996)

12. G. D. Boreman, C. Fumeaux, W. Herrmann, F. K. Kneubuehl, H. Rothuizen, "Tunable polarization response of a planar asymmetric-spiral infrared antenna," Opt. Lett. **23**(24), 1912-1914 (1998)

13. F. J. González and G. D. Boreman, "Comparison of dipole, bowtie, spiral and log-periodic IR antennas," Infrared Phys. Technol. **46** 418$-$428 (2005)

14. C. Fumeaux, W. Herrmann, H. Rothuizen, P. De Natale, and F. K. Kneubuehl, "Mixing of 30 THz laser radiation with nanometer thin-film Ni$-$NiO$-$Ni diodes and integrated bow-tie antennas," Appl. Phys. B **63**, 135-140 (1996)

15. C. Fumeaux, M. A. A. Gritz, I. Codreanu, W. L. Schaich, F. J. Gonzalez, and G. D. Boreman, "Measurement of the resonant lengths of infrared dipole antennas," Infrared Phys. Technol. **41**, 271-281 (2000)

16. E. N. Grossman, L. R. Vale, D. A. Rudman, K. M. Evenson, and L. R. Zink, "30 THz mixing experiments on high temperature superconducting Josephson junctions," IEEE Trans. Appl. Supercond. 5(2), 3061$-$3064 (1995)

17. M. E. MacDonald, E. N. Grossman "Niobium microbolometers for far-infrared detection," IEEE Trans. Microwave Theory Techn. MTT-43(4), 893-896 (1995)

18. J. G. Small, G. M. Elchinger, A. Javan, A. Sanchez, F. J. Bachner, and D. L. Smythe, "AC electron tunneling at infrared frequencies: thin-film M-O-M diode structure with broad-band characteristics," Appl. Phys. Lett. **24**(6), 275-279 (1974)

19. I. Wilke, Y. Oppliger, W. Herrmann, and F. K. Kneubuehl, "Nanometer thin-film Ni$-$NiO$-$Ni diodes for 30 THz radiation," Appl. Phys. **A58**, 329-341 (1994)

20. E. N. Grossman, T. E. Harvey, and C. D. Reintsema, "Controlled barrier modification in Nb/NbOx/Ag metal insulator metal tunnel diodes," J. Appl. Phys. **91**, 12, 10134$-$10139 (2002)

21. E. D. Palik, *Handbook of Optical Constants of Solids, Volume 1*; New York, Academic, 1980.

22. E. N. Grossman, J. A. Koch, C. D. Reintsema, A. and Green, "Lithographic dipole antenna properties at 10 μm wavelength: comparison of method-of-moments predictions with experiment," Intl. J. Infrared Milli. **19**, 6, 817-825 (1998)

23. J. G. Simmons, "Electric tunnel effect between dissimilar electrodes separated by a thin insulating film," J. Appl. Phys. **34**, 9, 2581-2590 (1963)

24. J. R. Tucker and M. J. Feldman, "Quantum detection at millimeter wavelengths," Rev. Mod. Phys. **57**, 4, 1055-1114 (1985)

25. A. Hartstein and Z. A. Weinberg, "Unified theory of internal photoemission and photon-assisted tunneling," Phys. Rev. B **20**, 1335 - 1338 (1979)

26. M. Heiblum, S. Wang, J. R. Whinnery, and T. K. Gustafson, "Characteristics of integrated MOM junctions at dc and at optical frequencies," IEEE J. Quantum Electron. **QE-14**(3), 159-169 (1978)

27. A. Hartstein, Z. A. Weinberg, and D. J. DiMaria, "Experimental test of the quantum-mechanical image-force theory" Phys. Rev. B **25**, 7174 - 7182 (1982)

28. F. E. Terman, *Radio Engineers' Handbook*, New York, McGraw-Hill, 1943, 211-212

29. Philip C. D. Hobbs, Robert B. Laibowitz, and Frank R. Libsch, "Ni$-$NiO$-$Ni tunnel junctions for terahertz and infrared detection," Appl. Opt. **42**, 32, 6813-6822 (2005)

30. P. C. D. Hobbs, "POEMS: a programmable optimizing electromagnetic simulator," http://www.watson.ibm.com/actj.html

31. S. J. McNab, N. Moll, and Y. A. Vlasov, "Ultra-low loss photonic integrated circuit with membrane-type photonic crystal waveguides," Opt. Express **11**, 22, 2927-2939 (2003)

32. K. Terakura, A. R. Williams, T. Oguchi, and J. Kuebler, "Transition-Metal Monoxides: Band or Mott Insulators," Phys. Rev. Lett. **52**, 20, 1830-1833 (1984)

1. Introduction

Infrared and terahertz detectors based on metal-insulator-metal (MIM) tunnel junctions coupled to metal antennas have been an area of modest but continuous research interest since the 1960s [1], [2]. MIM devices are very fast, with intrinsic tunnelling times of the order of 1 fs or faster [3], [4], [5], and should have very high quantum efficiencies as detectors, due to a lack of competing branches. They have been shown to have extreme electrical bandwidths as well [6]. With modern lithography, the required fine features can be made in large arrays if needed, and since only metal and metal oxide are required, they should be easy to add on top of existing CMOS circuitry. All these properties make antenna-coupled tunnel junction (ACTJ) devices attractive as detectors in infrared imaging and optical communication applications.

The principal reason that these devices have not been widely used is their very low efficiencies[7]. At 10.6 μm, where metal losses are much lower, even careful work has not yielded efficiencies above 0.1% in a tunnelling device; Wilke *et al.*[8] show a detected photocurrent of about 90 nA with a dipole antenna 4 μm long with an incident flux of 180W/cm^2, corresponding to an overall quantum efficiency below 0.05%. Abdel-Rahman *et al.*[9] show a device using a 90-Ω Ni—NiO—Ni junction with a noise-equivalent power (NEP) of 180 pW/$\sqrt{\text{Hz}}$ at 10.6 μm, which would correspond to an overall quantum efficiency of about 0.9%, but their I-V curves have the wrong sign of nonlinearity for tunnelling (the junction resistance increases at higher bias, rather than decreasing), which shows that these devices are actually not tunnel junction detectors at all.

Kale [10] pointed out that the low observed efficiencies of ACTJ devices could be expressed as the product of four separate contributions,

$$\eta = \eta_a \eta_s \eta_c \eta_j, \tag{1}$$

where η_a is the antenna efficiency (actual collected power/intercepted power), η_s is the efficiency of conducting the resulting electric current down the antenna to the feedpoint, η_c is the matching efficiency between the current in the antenna and the junction, and η_j is the internal quantum efficiency of the junction. Boreman *et al.*[11], [12], Gonzalez and Boreman [13], Fumeaux *et al.*[14], [15], Grossman *et al.*[16], and Macdonald *et al.*[17] have done extensive numerical and experimental work on infrared antennas coupled to niobium bolometers, and Small *et al.*[18], Wilke *et al.*[19], Fumeaux *et al.*[14], [6], and Grossman *et al.*[20], with antenna-coupled MIM tunnel junctions, so that the state of knowledge of these efficiency factors and their relative importance is gradually improving. The Boreman group has produced thin film antennas with $\eta_a\eta_s \approx 0.46$ at 10.6 μm with bolometric detection, confirming an earlier result of Grossman *et al.*, who claimed approximately 50% antenna efficiency with bolometric detection. These mid-infrared results are not directly applicable to the near infrared, because of the extreme dispersion of the optical constants of metals in that region. For instance, between 10 μm and 1.5 μm, the refractive index of nickel drops from 7.11 +i38.3 to 3.38+i6.82, and that of copper from 10.8+i47.5 to 0.606+i8.26 [21]. These values are too low, and their phase angles too far from the normal conductor value of $\pi/4$, for the usual low frequency antenna design methods (e.g. moment methods) to give accurate results, though there is some resemblance between method-of-moments predictions and experiment in the 11-μm band [22].

Although these devices are applicable from dc to at least 200 THz, the appropriate description of their detection physics is not the same throughout this range. At low frequency, the incident electromagnetic wave produces an ac voltage across the tunnel junction, causing the instantaneous bias voltage to change, and walking the junction up and down its I-V curve, which is correctly predicted by semiclassical theory[23]. Where the photon energy $h\nu \leq eV_f$ (where V_f is the typical turn-on voltage of the junction), photon-assisted tunnelling produces lumps in the I-V curve. In the present case, where $h\nu \approx 0.8$ eV and $V_f \approx 0.1$ V, the enhanced conductance

due to illumination is best described as internal photoemission over the tunnel barrier[24], [25]. Fortunately, in many respects the internal photoemission results are similar to those predicted by semiclassical square well tunnelling theory modified by the classical image potential [23], [26], [27], so to first order, one can design infrared ACTJ devices using the low-frequency circuit model.

In this model, η_c is determined by the impedance matching of the junction resistance to the antenna radiation resistance. Typical antennas have radiation resistances of the order of 30-300 Ω, so the total resistance at the feed point of the antenna is about 15-150 Ω. In order to achieve high efficiency in the near IR by impedance-matching to the antennas, junction areas less than 0.05 $(\mu m)^2$ are required to minimize capacitance. To impedance-match to an antenna at that area requires a very low resistance-area (RA) product, on the order of 1 $\Omega(\mu m)^2$, requiring thin tunnel oxides with low barriers. The Ni$-$NiO$-$Ni junction, with its 0.2 eV barriers, is the only known system capable of reaching 1 $\Omega(\mu m)^2$. Using nickel antennas makes it easy to grow NiO and thus allows high η_c, but unfortunately nickel is very lossy in the infrared, especially at shorter wavelengths, which means that η_s is very low for a nickel antenna.

Junction capacitance and conductance both scale as the junction area, so their ratio (the RC time constant of the junction) is area-independent, with a value

$$\tau = \frac{\varepsilon_0 \, \varepsilon_r RA}{d} \tag{2}$$

The relative dielectric constant ε_r seen by the tunnelling electrons is about 8.4, and all these junctions are very close to 2.5 nm thick [29]. Thus the time constant of a 1 $\Omega(\mu m^2)$ Ni$-$NiO$-$Ni junction is essentially constant at 30 fs irrespective of junction area. Assuming a one-pole RC transfer function, this will produce a rolloff of

$$|H(v)| = \sqrt{\frac{1}{1 + (2\pi v \tau)^2}}. \tag{3}$$

Note that the 3 dB point occurs where $v = 1/(2\pi\tau)$, i.e. when τ corresponds to 1 radian at frequency v. A 30-fs τ is 6 full cycles of 200 THz (37.7 rad), so the rolloff is $\approx$ -32 dB optical or -63 dB electrical. This disastrously large loss must be overcome if highly efficient ACTJ devices are ever to be built in the near IR. The two usual radio-frequency methods for doing so are reactive matching networks and travelling wave structures. In order for the reactive network not to dominate the loss, it would have to have an unloaded Q value of at least 50-100 [28], which is realizable at radio frequency but would be very difficult to realize in a metal structure in the infrared. Thus a travelling wave structure as used in this paper appears to be the only feasible method. It has the additional advantage of being much wider band than a high-Q resonance.

Hobbs *et al.*[29] showed experimental and theoretical results on the barrier heights and responsivities of the Ni$-$NiO$-$Ni system which suggest that these devices might exhibit responsivities of > 1 A/W in the infrared, and provided a self-aligned shadow mask fabrication method suitable for technological applications such as optical communications. In this paper, we present waveguide-integrated near-infrared detectors based on Ni$-$NiO$-$Ni junctions coupled to silicon strip waveguides via antennas. The antennas are made of a multilayer nickel-gold stack that combines the good infrared properties of gold with the very low tunnel barriers of the Ni$-$NiO$-$Ni system. They use a novel plasmonic waveguide at the feed point of the antenna, in which the tunnel junction is oriented transversely to the propagation direction of the fields, so that the detection is done in a travelling wave region and junction capacitance is therefore not a limitation.

Although these devices are not yet highly optimized, they show promise as detectors because of their practically unlimited speed and reasonable sensitivity, which is $1-2$ orders of magnitude greater than that of previously reported devices.
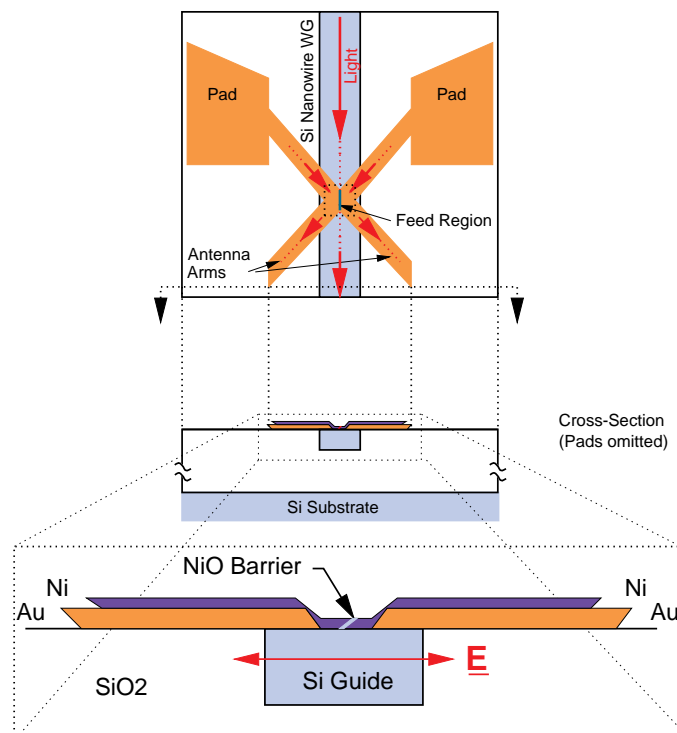

Fig. 1. Outline drawing of the waveguide, antenna, and tunnel junction structure. The waveguide is 0.45 μm wide and 0.22 μm tall.

2. Device design and fabrication

The device used here is shown schematically in Fig. 1. Light comes in down a rectangular silicon nanowire waveguide of 0.45-μm width and 0.22-μm height. It encounters a coupling structure consisting of two gold V-antennas arranged back-to-back, with a 300 nm long plasmonic waveguide between them. The plasmonic waveguide includes a Ni$-$NiO$-$Ni edge junction structure along its entire length, and thus functions as a travelling-wave detector. Although this structure is only about 0.4 μm long, the plasmon wavelength is so short that this corresponds to more than two complete cycles.

The waveguides are 0.45 μm wide and 0.22 μm tall, with a SiN top cladding of about 20 nm and a SiO$_2$ bottom cladding of 2.0 μm. They are fabricated from bonded silicon-on-insulator (SOI) wafers, and planarized via a nearly standard shallow-trench isolation (STI) process, in which high density PECVD (HDP) oxide is deposited, densified, and polished back to form a surface coplanar with the waveguide top surface.

The ACTJ process flow is closely similar to the self-aligned process of Hobbs *et al.*[29], with the addition of alignment features. It uses angled directional metal evaporation through a germanium shadow mask supported by a 700-nm layer of polymethyl methacrylate (PMMA), which is undercut by reactive-ion etch (RIE) to form suspended bridges. This allows excellent
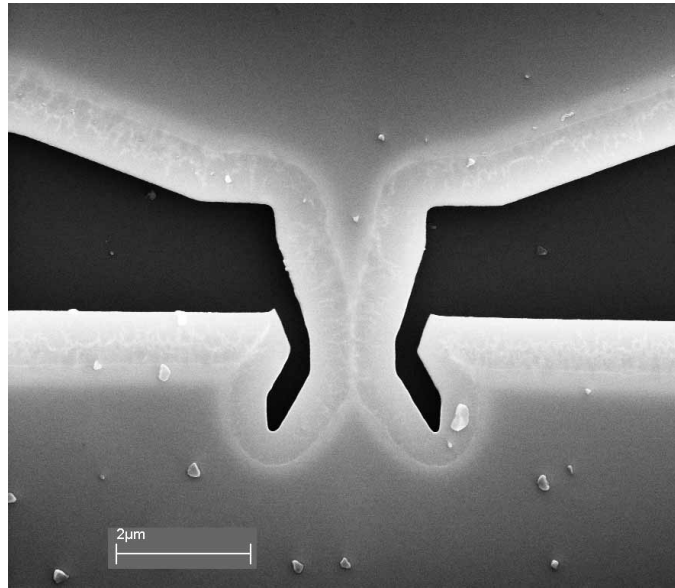
Fig. 2. SEM of a Ge shadow mask on the wafer used in Fig. 4, after Ge and PMMA etch steps, but before metal deposition. The undercut region is clearly visible through the 50-nm Ge layer, as is PMMA residue adhering to the bottom of the Ge.
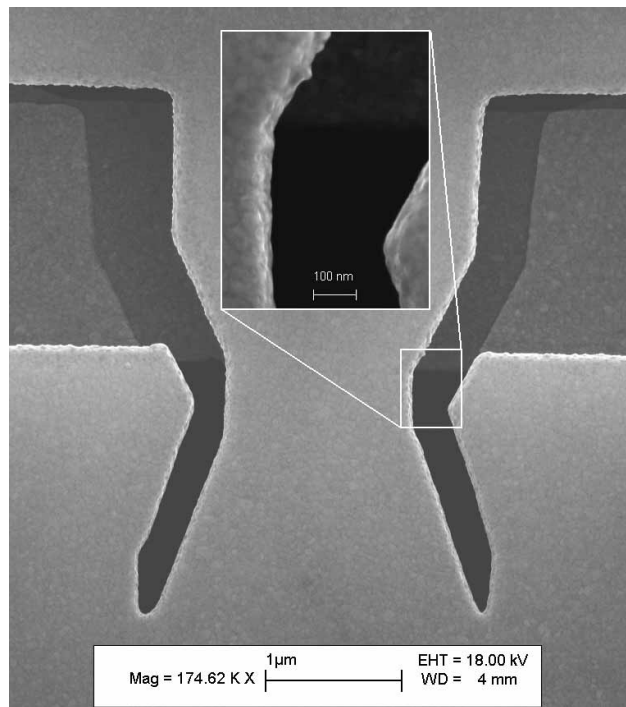

Fig. 3. A bridge structure from the same wafer as that of Fig. 4, after the Ni adhesion layer and two 60-nm gold evaporations. The undercut and bottom-side resist residue are now invisible beneath the thick metal.

control of overlap area and feature position; an angular error of $1°$ from an incidence angle of $40°$ produces a position error of only 21 nm. Furthermore, keeping the junctions away from the photoresist improves junction quality and yield. Beginning with a wafer containing planar waveguides, 248-nm deep-UV (DUV) lithography and liftoff are used to deposit gold alignment marks for electron-beam processing; gold marks, unlike silicon ones, are easily detectable through the overlying layers. The 700-nm PMMA layer is spun on, and 50 nm of Ge applied by electron-beam evaporation. The bridge pattern is applied by normal e-beam lithography, followed by dicing into pieces consisting of several chips. The bridges are then made by etching the Ge in a CF_4/Ar RIE, and the PMMA is undercut by an O_2 RIE that also ashes the e-beam resist, leaving the suspended structure shown in Fig. 2.

The antenna structure consists of six images of the apertures in the Ge mask, three from the left and three from the right. In order to make the gold stick to the oxide/nitride surface, two 2-nm Ni adhesion layers are put down first, at angles symmetric about the normal. Next come two 60-nm Au layers, at the same angles as the Ni, which form the arms of the antennas. The angles are chosen to leave a small ($\approx$100 nm) gap between the antenna arms to avoid short circuits. Then the lower Ni layer is deposited, 25 nm thick, and at a more oblique angle so as to cross the centre line of the waveguide by approximately 40 nm. The sample is then removed from the chamber for oxidation. It is important that the sample not be allowed to overheat; temperatures above about 70°C cause increased outgassing from the PMMA support layer, resulting in poor metal morphology and significant blurring of the features due to gas collisions.
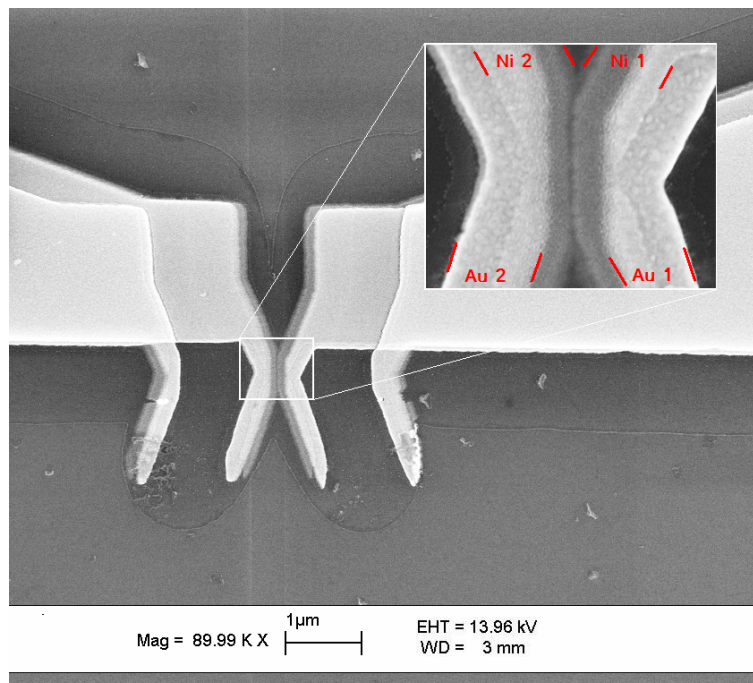

Fig. 4. SEM of one of the devices used in this work. The faint vertical stripe is the Si waveguide; lightest areas gold, and darker areas Ni and bare substrate. The extent of the undercut in the PMMA support layer (before liftoff) is visible as a line of carbon residue. The extra antenna arms outside the waveguide region are useless but harmless, and result from the multiple-angle deposition technique.

The junction oxide is grown in a very gentle oxygen plasma (20 mT O_2, 10 W RF, 5 s) in a

Unaxis 790 RIE tool, after which the sample is replaced in the evaporator for the final 25-nm Ni layer, which forms the top of the edge junction.

Figure 3 shows the bridge structure after the adhesion layers and the two Au layers. Even though the metal is more than twice as thick as the Ge bridge, there is no apparent tendency for the bridges to warp due to stress. Slight narrowing of the apertures in the Ge is expected due to metal buildup.

Figure 4 is a scanning-electron micrograph (SEM) of a device on the chip used in this work. The sloped edges of the two Ni layers overlap to form an almost perfect edge junction. The outline of the undercut region is visible from the carbon residue left behind; it is is similar in shape to that visible through the Ge mask of Fig. 2.

This structure was designed using an optimizing finite-difference time domain (FDTD) electromagnetic simulator. This "Programmable Optimizing Electro-Magnetic Simulator" (PO-EMS) [30] can take a parameterized description of a family of devices and optimize for any desired property. In this case, the simulations showed that there was more to achieving high η_c than just impedance matching—it is vitally important not to try to force the optical-frequency currents to turn corners, as this leads to huge losses. The present structure maintains *TE* field orientation throughout, including the use of true edge junctions rather than overlaps.

Because of process variations and the buildup of metal on the edges of the holes in the shadow mask, the antennas actually built are somewhat different from the design, but we anticipate that an adjusted photomask will correct for these and allow us to build these optimized antennas and plasmonic travelling wave structures.
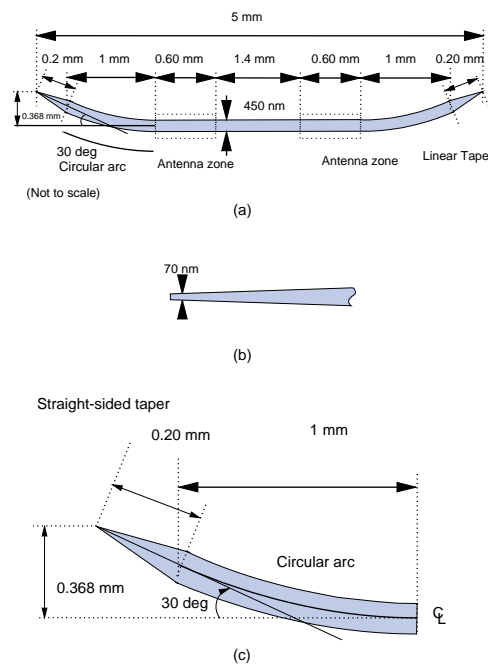

Fig. 5. Waveguide layout showing curves and adiabatic tapers for coupling into polymer waveguide. (a) Layout of each waveguide; (b) detail of taper point; (c) detail of curve and taper.

2.1. Waveguide coupling

The waveguide pattern used here is shown in Fig. 5. The waveguides are crystalline silicon strip guides of 0.45-μm width and 0.22-μm height, planarized with SiO$_2$ cladding on the top and sides, providing very low sidewall roughness $< \approx 3$ nm rms. The top cladding is approximately 20 nm of Si$_3$N$_4$ remaining from the polishing process used in planarization. In order to avoid artifacts due to substrate light, each guide has a 30°bend at both ends. The last 200 nm of each guide is a linear adiabatic taper, ending in a point between 30 nm and 60 nm wide, designed to couple into a 3-μm square polymer waveguide, as in McNab *et al.*[31].
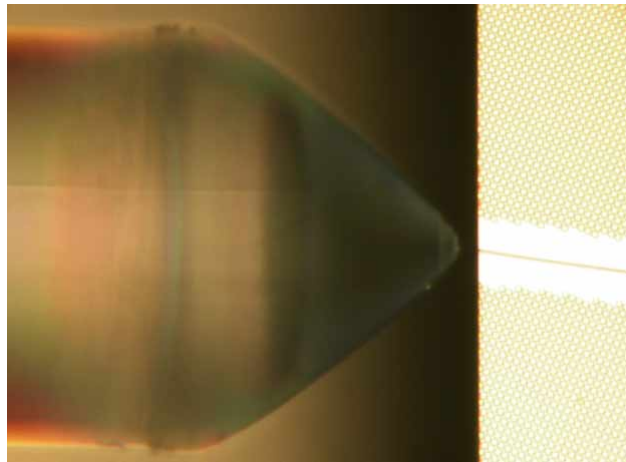

Fig. 6. Optical micrograph showing one end of the coupling structure, with the lensed tapered optical fibre at left, and the silicon waveguide as the very small line at right, between the two areas of fill pattern. This shows a cleaved edge, which did not quite reach the straight region of the guide.

Since the polymer coupling process was still under development, we cleaved the chip through the straight portion of the waveguide, and used lensed tapered fibres for coupling (Oz Optics Ltd. TPMJ-3S-1550-8/125-0.4-10-2.5-14-2-AR), as shown in Fig. 6. Measurements using two of these fibres to measure the end-to-end coupling of another waveguide from the same wafer, but without an antenna, showed an overall mean coupling loss of 28.3 ± 1 dB. Apportioning the loss equally to both ends, we calculate the power in the waveguide incident on the antennas as 14.1 ± 0.7 dB below the power in the input fibre.

3. Experimental results

3.1. Low-frequency behaviour

Figure 7 shows a measured current-voltage (*I-V*) plot of one of the detector junctions, together with the *I-V* curve calculated from the fitted function. Junction parameters shown were extracted from the experimental *I-V* curve by fitting the general Simmons equation using the same procedure as in Hobbs *et al.*[29]. As stated above, it has been commonly thought that due to the intrinsically high speed of the tunnelling process, the infrared behaviour of these MIM junctions should be similar to their DC behaviour, particularly as regards responsivity vs bias.

Figure 8 is a plot of the calculated junction behaviour, including current, junction resistance, resistance nonlinearity, and junction responsivity, all as a function of bias, calculated from the fit of Fig. 7. This assumes that the DC and infrared responses are the same, as mentioned above.

Tunnelling Eqn Fit to eb02b1det.dat

A(μm^2): 0.01192 K: 8.3380 ϕ_1(eV): 0.1884 ϕ_2(eV): 0.2257 T(Å): 25.350566 $R_s(\Omega)$: 1080 ε_{rms} 0.347759%
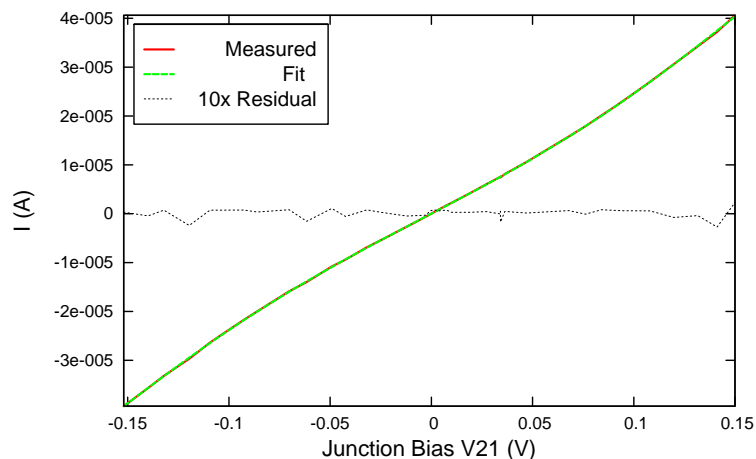
Fig. 7. Current-voltage plot of a waveguide-integrated detector, with a Simmons-equation fit. V21 is the bias voltage across the junction.

Tunnel Current Calculation

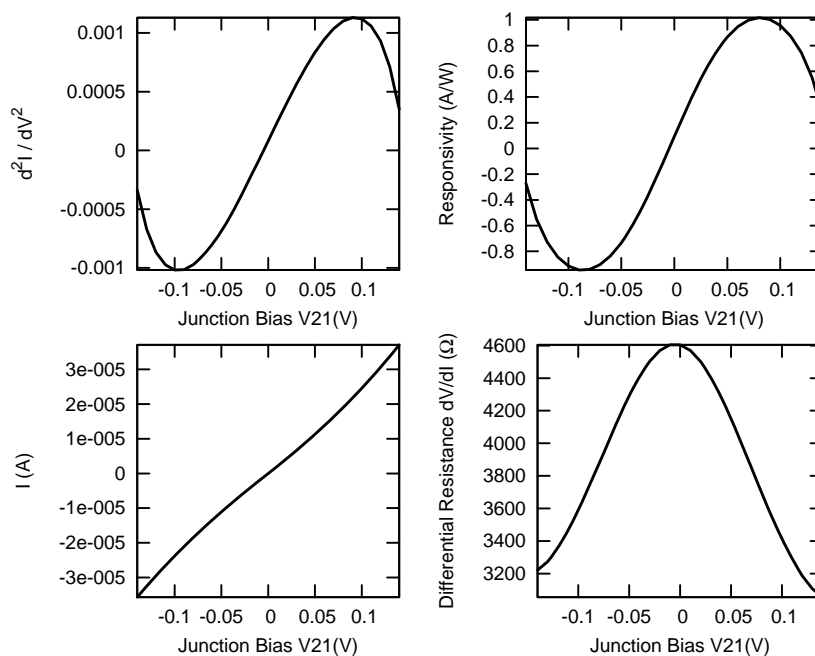A(μm^2): 0.01192 K: 8.3379 ϕ_1(eV): 0.1884 ϕ_2(eV): 0.2257 T(Å): 25.351000 $R_s(\Omega)$: 1080

Fig. 8. Junction resistance and optical responsivity (in the impedance-matched condition) calculated from the DC I-V curve fit of Fig. 7.

The slight asymmetry is due to the top and bottom junctions having slightly different barrier heights [29].
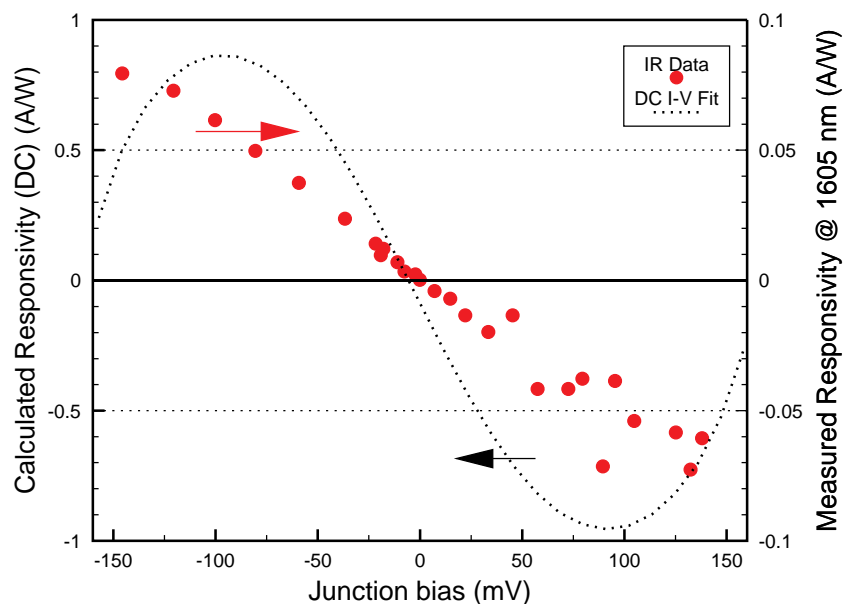

Fig. 9. Total responsivity vs bias, for 27 μW @ 1.605 μm incident in the Si waveguide. End-to-end quantum efficiency is over 6%, which is 1-2 orders of magnitude higher than previously reported devices. The dashed curve is derived from a fitting procedure like that in Fig. 8.

3.2.   Optical detection

Figure 9 is a plot of detected signal vs bias voltage for chopped 1.605 μm light, for a $\approx$ 400-Ω junction. These data were taken using an external cavity diode laser, mechanical chopper, and lensed tapered single-mode fibre coupling. The responsivity R is calculated as

$$R = \frac{\Delta V_j}{r_j P_g} \qquad (4)$$

where ΔV_j is the measured change in junction voltage due to the incident light, r_j is the differential junction resistance, calculated as a divided finite difference of the $I - V$ curve, and P_g is the optical power incident in the silicon waveguide, which in this case is 27 μW (after accounting for the 14.1 dB fibre-to-waveguide coupling loss).

The signal polarity is opposite to that of the bias, which is as expected for tunnelling detection. Optical stimulation increases the junction conductance; with constant external bias current, this produces a decrease in junction forward voltage. Bolometric detection, in which Joule heating from the optical currents increases the load resistance, produces an output of the same polarity as the bias when dominated by the temperature coefficient of the metal, and of the opposite polarity when dominated by that of the junction. Since the metallization of these devices has a low resistance (a few ohms), there is probably some thermal contribution to the tunnelling detection.

The maximum responsivity is 0.080 A/W, which represents a total quantum efficiency η of 6%, the highest value ever reported for an ACTJ detector. (Other devices from the same wafer

also had similar efficiencies.) This efficiency includes all of Kale's factors: η_a for electromagnetic coupling from the Si waveguide into the antenna, η_s for the metal conduction, η_c for the mode matching to the junction, and η_j for the efficiency of the junction itself. Efficiencies of this order, while not yet competitive with semiconductor detectors, are already technologically useful. Since the antennas are very small, the capacitance of these detectors is also very low, approximately 300-600 aF, and they are expected to be very fast as well, being made in the same material system as Fumeaux's 176 GHz devices.
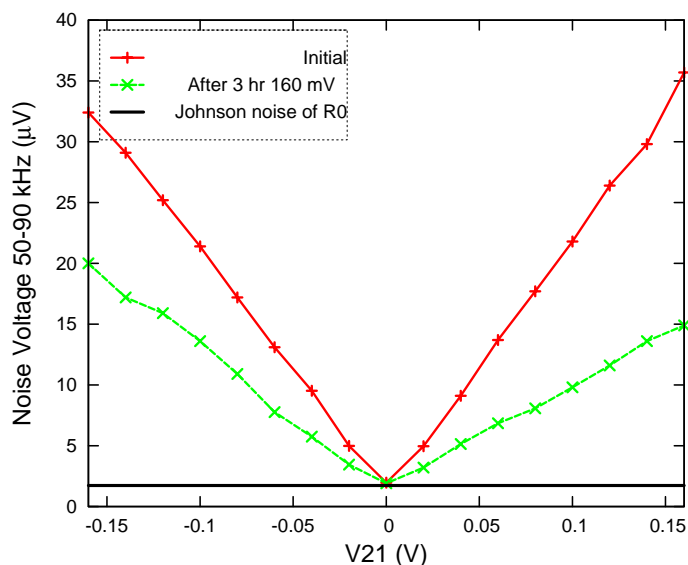

Fig. 10. Low frequency (50-90 kHz) noise voltage of a 4500-Ω junction. similar to that of Fig. 8. The noise has a 1/f character.

3.3. Noise behaviour

The responsivity of a detector is only half the story. In order to determine the usefulness of these devices, we have to take account of their noise properties. Figure 10 shows the low frequency noise voltage of the device of another junction from the same run with a zero-bias resistance of 4.5 kΩ, plotted vs. bias level. The noise increases approximately linearly with bias, and shows a pronounced $1/f$ noise peak, whose shape and amplitude are time-dependent. The quoted bandwidth of 50-90 kHz was chosen to avoid spurious signals due to stray pickup. These devices are Johnson-noise limited above the $1/f$ noise corner at about 5 MHz. For a 400-Ω junction, this corresponds to a noise equivalent power of 80 pW/$\sqrt{\text{Hz}}$ at 1.6μm.

It appears that the $1/f$ noise is predominantly of magnetic origin. Because nickel is ferromagnetic, and the lowest empty band of nickel oxide is a spin-polarized D band [32], the conductance of the junction depends on the magnetization of the nickel. More work is needed to characterize this effect, but in the present case, holding a rare earth magnet near the device under test caused its 1/f noise to disappear, leaving it Johnson-noise limited even at audio frequencies. This useful effect is of course irreversible, so the data shown are for another junction from the same run.

4. Discussion and further work

The results presented clearly show that it is possible to build efficient antenna-coupled tunnel junction infrared detectors at wavelengths as short as 1.6 μm. Unlike semiconductor devices, MIM tunnel junctions are not frequency selective, having broadband responses from DC to at least the near IR. Their very low capacitance and high speed makes them attractive as detectors for optical interconnection, and their simplicity makes them easy to integrate on top of standard IC processes. Now that it is known that technologically useful responsivities can be achieved with these devices, their field of application should widen considerably in image sensors, optical interconnection, optical mixing, and other areas.

Previously reported results in the 10-μm band have shown excellent efficiencies from antennas coupled with metal microbolometers and very poor efficiencies when ACTJ devices are used. This has led many to conclude that the inefficiency is an inherent property of the tunnel junction device itself. The present work has shown that the inefficiency in previous ACTJ devices lay primarily in the poor choice of antenna metal (Ni alone), and too little attention to the mode matching efficiency η_c (overlap junctions with quasi-lumped element junctions). The combination of Au/Ni antennas, plasmonic travelling wave detector design, and true edge junctions leads to far higher efficiencies, which shows that the junctions themselves are inherently efficient, as might be expected from first principles. Although Ni-NiO-Ni devices have been shown to be extremely fast in mid-infrared measurements, nevertheless the baseband measurements presented here do not rule out thermal contributions to the detector responsivity, so our future work will focus on new material sets and higher speed measurements.

4.1. Process improvements

The devices used here were made by e-beam lithography, which though it is a flexible and capable research tool, is far too slow to be used in mass-production parts. Deep-UV lithography works well at the feature sizes of these structures; however, most DUV photoresists require bottom antireflection coatings (ARCs) that must be baked at temperatures above 150 °C to crosslink them and prevent the ARC from dissolving in the resist. Since the glass transition temperature(T_g) of PMMA is only 105 °C, this bake melts the PMMA and crazes the germanium. Since it has proved difficult to find a suitable replacement for the ARC, work is now underway to replace the PMMA with a higher-T_g polymer, which will permit the use of normal DUV lithography.

There are several serious hindrances to the achievement and validation of accurate theoretical models of real ACTJ devices. One is the poorly known infrared optical constants of thin metal films, which frequently have low-frequency conductivities a factor of two or more below the bulk value at room temperature. Another is the highly sensitive interaction of surface plasmon coupling with small device geometry variations. Nonetheless, as we have demonstrated in this paper, it is possible to make useful devices in spite of this uncertainty.

Having to break vacuum to form the barrier oxide is not ideal from a process control and device lifetime standpoint; ambient exposure time and relative humidity are difficult to control, and trace contaminants such as sulfide and oils may get into the junctions, potentially causing variability or unreliability. In-situ oxidation in the evaporator would probably give improved process control by keeping the metal-oxide interface clean. One of the potential benefits of this self-aligned shadow mask process is that such a unitary vacuum process is possible, but it will require equipment modifications.

Finally, improved coupling into the waveguide requires a proper coupling structure. We are currently implementing a wafer-level process for fabricating adiabatic inverse taper couplers similar to those of McNab *et al.*[31], which we expect to reduce the coupling loss to 1-2 dB, which will reduce the uncertainty in the coupling proportionately.

5. Conclusion

In this paper we have presented a new optical detection technology based on MIM tunnel junctions coupled to silicon nanowire waveguides via multimetal thin-film antennas. These devices have for the first time shown detection sensitivities high enough to be of technological interest in the 1.5-μm band, and it appears quite likely that further significant efficiency improvements can be obtained by optimizing the device design. The advances which led to this improvement are the addition of multi-metal antennas optimized using FDTD methods, a plasmonic travelling wave detection region to eliminate junction capacitance, true edge junctions to improve mode matching between the junction and the antenna, and integration with silicon nanowire waveguides. These advanced devices are nonetheless easily fabricated in a CMOS-compatible process, and so hold great promise in optical interconnection and other areas.